Materials Research Express

OPEN ACCESS

RECEIVED
15 October 2025

REVISED
24 November 2025

ACCEPTED FOR PUBLICATION
18 December 2025

PUBLISHED
5 January 2026

PAPER

Biosynthesized nickel oxide honeycomb nanostructures for DSSC counter electrode: a joint experimental and density functional theory study

Stella Nasejje[1], Emmanuel Mushebo[1], Denise Joanitah Birabwa[2], Mmantsae Diale[3] and Emma Panzi Mukhokosi[1,*]

[1] Department of Physics, Faculty of Science, Kyambogo University, PO Box 1, Kyambogo, Uganda
[2] Department of Electrical and Electronic Engineering, Kyambogo University, PO Box 1, Kyambogo, Uganda
[3] Department of Physics, University of Pretoria, Private Bag X20, Hatfield 0028, South Africa
[*] Author to whom any correspondence should be addressed.

E-mail: epmukhokosi@kyu.ac.ug

Keywords: nickel oxide, biosynthesis, dye-sensitized solar cells (DSSC), bamboo shoot, DFT

Abstract

The urgent need to address fossil fuel challenges has led to a surge in green energy technologies, including solar cells. Nanodimensional particles, particularly 2D nanostructures, have shown great potential in these technologies due to their high surface area-to-volume ratio. Nickel oxide (NiO) is a promising p-type semiconductor for solar cell photo-cathodes, offering remarkable physical and chemical properties at a relatively low cost. However, its surface morphology, area, and pores have a significant impact on performance. Traditional chemical synthesis methods for NiO nanostructures have several drawbacks, including the use of hazardous precursors. To address this, we present for the first time a novel bioengineering method using bamboo shoot extract to produce 2D NiO nanostructures. The results have been supported by Density Functional Theory (DFT) calculations. The DFT calculations revealed that NiO is a p-type semiconductor with direct band gap for spin-down at Γ. The results show that the bioengineered NiO nanostructures exhibit high crystallinity and a honeycomb-like morphology. We successfully integrated these nanoparticles into a dye-sensitized solar cell (DSSC), demonstrating their viability as a counter electrode. The cell exhibits promising performance, with a short-circuit current density of 0.113 mA cm^{-2} and an efficiency of 0.0057%. This study presents a straightforward, cost-effective, and environmentally friendly method for bioengineering NiO honeycomb-like nanostructures, thereby paving the way for sustainable energy solutions.

1. Introduction

Green energy technologies are thought of as an urgent solution in the bid to realize the carbon-zero target to curb the challenges of fossil fuel usage [1]. Dye-sensitized solar cells (DSSCs) have attracted attention as a promising renewable energy technology due to their low cost, simple procedures for their assembly, and having a high efficiency compared to traditional silicon solar cells [2].

A DSSC comprises of a working electrode (Photoanode—usually TiO_2), dye molecules (photosensitizer to enhance solar absorption), a redox couple electrolyte (usually an iodide/triiodide, I^-/I_3^- solution), and a counter electrode (photocathode- usually platinum, Pt) [2–4]. Research studies have been carried out on different DSSC components so as to improve on their performance. The counter electrode's pivotal role is to collect electrons from the external circuit and transfer them to the electrolyte so as to catalyze the redox reaction leading to regeneration of the oxidized dye molecules [3, 5, 6]. Platinum (Pt) boosts with a high electrical conductivity of about 9.43×10^6 Sm^{-1} and catalytic properties, hence its significant application as a counter electrode in DSSCs [6]. However, Pt's high cost at about 4.6 USD per m^2 of a 5 nm-thick Pt film renders it expensive for commercial DSSC production and thus the need for studies into its replacement materials [6].

The use of metal oxide semiconductors such as titanium dioxide (TiO_2), tungsten trioxide (WO_3), hematite (α-Fe_2O_3), nickel oxide (NiO), zinc oxide (ZnO), and copper oxide (CuO) among others as photoelectrode materials provides an exceptional reason for DSSCs being an eco-friendly and cost effective means for conversion of solar energy into electrical energy [2, 4].

P-type oxides, once used as counter electrodes, can act as efficient hole transport layers [5]. Nickel oxide (NiO), a p-type semiconductor (S.C.) with a cubic crystal structure, has a wide band gap (~3.4–3.8 eV) and is assigned to the charge transfer electronic transition of $O2p \rightarrow Ni3d$ [7, 8]. It has good optical properties, electrochemical stability, and is relatively low in cost, while also boasting excellent durability. These remarkable physical and chemical properties have enabled NiO's extensive application in green energy technology fields such as supercapacitors, solar cell photocathodes, lithium-ion storage, photoelectrochemical devices, and cytotoxic activity, among others [9–11]. It must be noted, though, that NiO's performance is greatly dependent on the morphology, surface area, and pore properties [12].

Several research works have been carried out on NiO nanoparticles (NPs) for these applications, growing them via chemical and biosynthesis mechanisms, deriving different nanostructures. For instance, Hong *et al* synthesized NiO NPs via the wet chemical method realizing a spherical morphology [13], Wang *et al* developed honeycomb-like NiO via hydrothermal synthesis [14], Nagamuthu and Ryu developed Ag/NiO honeycomb structure via chemical method [15], Ren *et al* synthesized NiO mesoporous honeycomb-like structure via hydrothermal synthesis [12], Iqbal *et al* synthesized agglomerated NiO NPs via green synthesis using *Rhamnus Virgata* leaf extract [16], Barzinjy *et al* biosynthesized NiO of a spherical shape with the agglomerated cluster using pomegranate juice extract [17], and Iqbal *et al* also biosynthesized spherically agglomerated NiO NPs using fresh Rhamnus triquetra leaf extract [18].

Although different researchers have synthesized NiO of the honeycomb-like morphology via chemical techniques, these techniques pose several disadvantages, including requiring the application of hazardous precursors, long reaction durations in synthesis, thus are relatively expensive due to the large energy used in the process, in addition to requiring sophisticated methods for their achievement [8, 13]. Therefore, to reach global carbon neutrality, there is a need for a simple and cost-effective synthesis method [19, 20]. On the other hand, biological techniques have been used to develop NiO NPs of a spherical morphology, though to the best of our knowledge, none have managed to realize the honeycomb-like NiO morphology. In addition to the biosynthesized NiO NPs, researchers have used different plant extracts like cloves (*Syzygium Aromatic*) extract [21], Arabic Gum [22], and *C. Viminalis* [23] for synthesizing NiO NPs for biological applications. The phytochemical constituents, like polyphenols and flavonoids in plant extracts, enable the reduction of metal ions into metal oxides with subsequent capping, preventing agglomeration. Bamboo shoots contain phytochemicals like phenols, terpenoids, flavonoids, and vitamins essential for metal reduction in biosynthesis [24, 25], thus, their fresh juice extract was used to biosynthesize NiO NPs for application as a photocathode in DSSC in this study. To this, we study the various structural and optical properties of the NiO NPs produced at different calcination temperatures −300 °C, 400 °C, and 500 °C, and examine the performance of the NiO photocathode in a setup with TiO_2 photoanode (TiO_2-NiO DSSC). For the theoretical studies, the structural, electronic, and optical properties on spin-polarized NiO have been investigated using density functional theory with Hubbard correction (DFT+U).

2. Methods

2.1. Materials

2.1.1. Experimental section

Fresh Bamboo shoots were obtained from the Mt. Elgon region in eastern Uganda. Nickel nitrate hexahydrate ($Ni(NO_3)_2 \cdot 6H_2O$), ethanol (98% purity), hexachloroplatinic powder, iodide, polyethylene glycol (PEG), Ruthenium dye (Ru N719), Fluorine-doped tin oxide (FTO) glass substrate, and deionized (DI) water were used. The chemicals were obtained from Sigma Aldrich suppliers and used with no further purification.

2.1.2. Theoretical section

The computational approach involved using the self-consistent plane wave open source code in the quantum ESPRESSO package, based on spin-polarised density functional theory (DFT) [26]. The generalised gradient approximation (GGA) exchange–correlation functional, provided by Perdew, Burke, and Ernzerhof (PBE), was employed, and norm-conserving pseudo potentials were utilised throughout the calculations for the ion-electron interaction [27]. The HUBBARD parameters U = 5 and 6 eV were applied as a Coulomb correction approach on the strongly correlated 3d orbitals of Ni, since they can give an improved description of the electronic structure as reported in previous literature [28, 29]. The cutoffs of 70 Ry and 280 Ry for kinetic energies and charge densities, respectively, were applied as a plane wave basis. The conversion threshold for

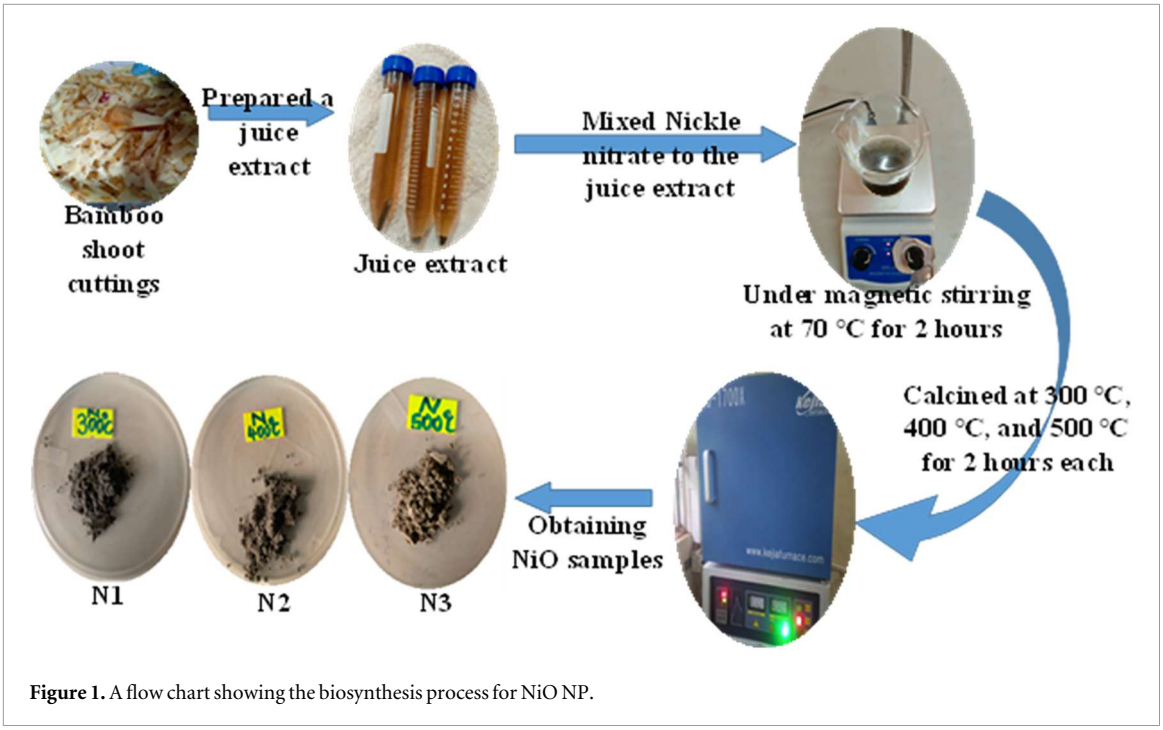

Figure 1. A flow chart showing the biosynthesis process for NiO NP.

energies and forces was set to 4×10^{-10} Ry and 0.001 Ry/Bohr. The Monhorst-Pack K-points mesh of $7 \times 7 \times 7$ and $14 \times 14 \times 14$ were sampled for structural optimization and electronic properties calculations. The optical properties of the anti ferromagnetic (AFM) NiO with strongly correlated 3d orbitals were correctly described by (1) [30].

$$E_{GGA+U} = E_{GGA}\frac{U-J}{2}\sum_{\sigma} T_r(\rho^{\sigma} - \rho^{\sigma}\rho^{\sigma}) \quad (1)$$

where J is the exchange energy (set at zero) and ρ^{σ} defines the spin (σ) polarized on-site density matrix of Ni atoms and the O-2s, O-2p, Ni-3d, Ni-3p, and Ni-4s were taken as the valence electrons in all the calculations.

2.2. Synthesis of the photoelectrodes

2.2.1. Extraction of juice from bamboo shoots

Fresh Bamboo shoots were cleaned thoroughly with distilled water, cut into small pieces, and blended into juice. 20 ml of the juice was added to 200 ml of deionized (DI) water and heated at 80 °C under magnetic stirring for 2 h. After cooling, the solution was sieved using a Whatman number 1 filter paper, obtaining a clear solution which was then centrifuged for 30 min at 3000 rpm, separating any residues from the required extract to get the plant extract solution for biosynthesis of NiO NPs.

2.2.2. Biosynthesis of NiO nanoparticles

4.0 g of nickel nitrate ($Ni(NO_3)_2 . 6H_2O$) was introduced to 100 ml of the plant extract and set under magnetic stirring at 70 °C for 2 h. The solution showed a gradual color change from brownish to dark green, indicating a reaction between the plant extract and the precursor. The final NiO solution was then dried in an oven at 110 °C for 12 h to obtain a powder, which was calcinated in a furnace at different temperatures of 300 °C, 400 °C, and 500 °C for 2 h each, giving the samples labeled as N1, N2, and N3, respectively, as shown in the schematics of figure 1. It was observed that the NiO NPs tend to differ in color, from dark grey towards light grey as calcination temperatures are increased from 300 °C to 500 °C.

2.2.3. Fabricating the NiO photo-cathode

0.2 g of NiO NP powder was added to a mixture of 0.15 g of polyethylene glycol (PEG), 2.5 ml of citric acid, and 2.5 ml of ethanol. The mixture was sonicated for 3 h, spin-coated onto an FTO glass substrate at 2000 rpm for 30 s, and left to dry on a hot plate at 70 °C for 5 min. Coating and drying were repeated eight times to achieve a desirable film thickness, which was then annealed at 400 °C for 2 h, obtaining the NiO photocathode.

2.3. Characterization

The crystallinity investigations on the synthesized samples were done using an x-ray diffractometer (SHIMADZU XRD 7000) with CuKα irradiation at $\lambda = 1.5406$ Å. The functional group analysis was carried

out using a Fourier transform infrared (FT-IR) spectrophotometer (SHIMADZU IRTracer-100) in the 400–4000 cm^{-1} wavenumber range. Scanning electron microscopy (SEM) using the ZEISS—Gemini 1 was carried out to establish the samples' morphology. Optical properties were studied using the diffused reflectance (DR) spectra measured using a UV–vis-NIR spectrophotometer (Cary 5000-model DRA-2500) over a 200–1200 nm wavelength range. The photoluminescence (PL) emission studies were carried out at room temperature with an excitation wavelength of 240 nm.

2.4. DSSC fabrication and performance evaluation

0.50 g of commercial TiO_2 powder was added to a mixture of 0.15 g of polyethylene glycol, 3 ml of glacial acetic acid and 3 ml of DI water to produce a paste that was sonicated for 3 h. The paste was spin-coated (to eight times) onto an FTO substrate and annealed at 400 °C for 2 h, obtaining the TiO_2 photoanode. Pt was drop-casted on the FTO substrate and annealed at 400 °C for 30 min to give the Pt counter electrode.

The iodide electrolyte was prepared by mixing 830.0 mg of potassium iodide powder with 27.0 mg of I_2 crystals in 10 ml of ethylene glycol under constant stirring for 30 min in the dark as described elsewhere [31–33]. The N719 Ru dye solution was prepared by mixing 10.0 mg of N710 dye powder in 15 ml of ethanol, under stirring for 8 h.

Two DSSC setups were fabricated. The TiO_2-NiO DSSC setup had a TiO_2 photoanode as a working electrode and a NiO thin film as the counter electrode. In this setup, the TiO_2 thin film was sensitized using the N719 dye for 24 h, rinsed with DI water, and left to dry. Using alligator clips, the TiO_2 and NiO thin films were joined in a sandwich, and an iodide electrolyte was injected between them to complete the DSSC.

In a similar way, with a photosensitized TiO_2 thin film sandwiched with a Pt counter electrode and an iodide electrolyte injected between them, the TiO_2-Pt DSSC setup was assembled.

To evaluate the DSSCs' performance, the *J-V* characteristics of the cells were evaluated by testing an active surface area of 0.25 cm^2 scanning from −1 V to +1 V at 10 mV step potential. This was carried out in a Photo Emission *J-V* measurements setup using a KEITHLEY 2450 Source Meter under 100 mA cm^{-2} illumination from a solar simulator (Ossila model, UK ltd).

Electrochemical impedance spectra (EIS) data were obtained for the DSSCs using a DC of 10 mV potential supplied using a Potentiostat (CORRTEST Instruments; Model: CS350M) at frequencies ranging from 1 MHz to 0.1 Hz. A 2-electrode configuration was used to supply the potential, and the cells were illuminated with a solar simulator at 100 mW cm^{-2} irradiance. The electrical resistances were characterized using Nyquist plots.

3. Results and discussion

3.1. Crystallinity investigations

The XRD patterns obtained for all NiO NPs samples gave sharp peaks of 2θ at about 37°, 43°, 63°, 75°, and 79° corresponding to (111), (200), (220), (311), and (222), respectively, as shown in figure 2. The patterns match well with the JCPDS card number 73 of space group $Fm\bar{3}m$ [34]. There is an observed peak shift to lower 2θ values with increasing calcination temperature. The peak intensities increase with increasing calcination temperature, indicating that higher crystallinity increases with calcination temperature.

The lattice parameters were calculated using the observed values for the (200) plane using the interplanar spacing (d_{hkl}) for the cubic structure exhibited by the NiO NP samples. Table 1 shows that the lattice parameter *a* reduces as the calcination temperature increases, indicating a contraction along the axes under increased temperature. These show a slight deviation from the standard value of the lattice parameter, $a = 4.1770$ Å, taken from the JCPDS card file data [35].

The Scherer formula shown in expression 2 was used to calculate the average crystallite sizes for all the NiO NP samples at major XRD peaks [36, 37].

$$D = \frac{0.9\lambda}{\beta \cos\theta} \tag{2}$$

where D is the crystallite size, β is the full width at half maximum (FWHM), and θ is the peak position. The crystallite values in table 1 indicate that increased calcination temperature reduces crystal defects in the NiO NPs.

The microstrain, ε, of the samples was calculated using expression 3.

$$\varepsilon = \frac{\beta}{4\tan\theta} \tag{3}$$

where β is the FWHM and θ is the peak position [36, 38]. These showed reducing microstrains with increasing calcination temperatures as indicated in table 1.

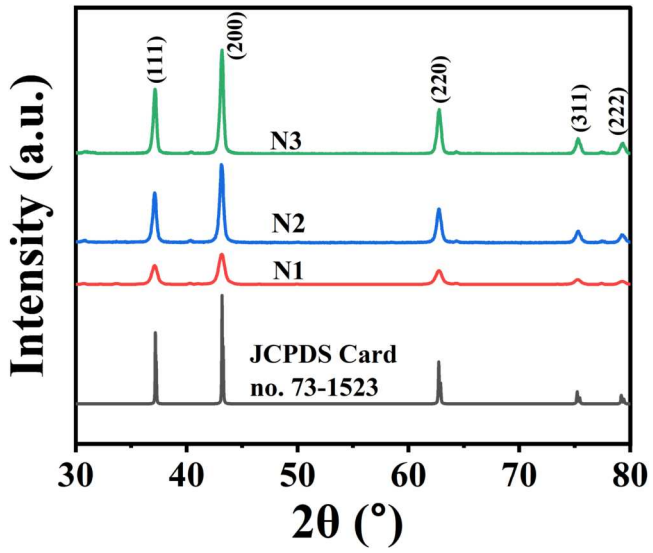

Figure 2. XRD patterns for biosynthesized NiO NPs calcined at different temperatures, with JCPDS standard spectra for NiO.

Table 1. Average crystallite properties for the NiO NP samples.

Sample	Interplanar spacing, d_{hkl} (Å)[$d_{hkl} = \frac{\lambda}{2\sin\theta}$]	Lattice parameter, a (Å) [$a = d_{hkl}\sqrt{(h^2 + k^2 + l^2)}$]	Crystallite size, D (nm)	Microstrain, ε ($\times 10^{-3}$)	Dislocation density, σ (nm^{-2})
N1	1.6930	4.1873	13.9383	5.6171	0.0054
N2	1.6928	4.1867	18.8353	4.0100	0.0028
N3	1.6922	4.1853	21.0170	3.5838	0.0023

The dislocation densities, δ of the samples, were evaluated using Williamson and Smallman's relation [36–38] shown in expression 4, obtaining reduced dislocation densities with increased calcination temperature as indicated in table 1.

$$\delta = \frac{1}{D^2} \tag{4}$$

3.2. Functional group analysis

All samples exhibited compound-specific peaks for Ni-O stretching in the fingerprint region at about 419.00 cm^{-1}, and 986.86 cm^{-1} for sample N1, at 405.27 cm^{-1}, 625.56 cm^{-1}, and 971.85 cm^{-1} for sample N2, and at 415.28 cm^{-1}, 605.53 cm^{-1}, and 971.85 cm^{-1} for sample N3 as shown in figure 3. The presence of the Ni-O stretching indicates that crystallinity in the synthesized NiO NPs was achieved, matching well with the XRD results. There is a possibility of the presence of the SP^3 C-O stretch in all samples shown at 1094.51 cm^{-1} for N1, and at 1079.49 cm^{-1} for both samples N2 and N3. An SP^2 C-O functional group is also present at a vibrational mode of 1363.20 cm^{-1} for N1, 1377.38 cm^{-1} for N2, and 1372.38 cm^{-1} for N3. Sample N1 has a carbon–oxygen double bond (C=O) at 1671.10 cm^{-1}, while samples N2 and N3 exhibited carbon–carbon double bonds (C=C) at 1646.07 cm^{-1} and 1641.90 cm^{-1}, respectively. All samples showed the existence of carbonized hydrogen stretches of Sp^3 C-H at 2819.27 cm^{-1}, 2814.27 cm^{-1}, and 2828.46 cm^{-1}. Samples N2 and N3 also exhibited the presence of hydrogen stretches of the O-H group in the vibrational region of 3669.57 cm^{-1}—2931.09 cm^{-1}, which is absent in sample N1. This suggests that for application in DSSCs, NiO NPs should be calcined to temperatures above 300 °C for the appropriate functional group to enable the transition of electrons in the photoelectrode semiconductor. The presence of these functional groups showed that NiO NPs interacted with proteins from the Bamboo shoot extract, verifying that the bioactive compounds led to the reduction and capping of NiO NPs.

3.3. Surface morphology studies

The SEM images show honeycomb-like morphology for the NiO NPs, as in figure 4. A soft topography is evident as shown in figures 4(a) and (b) for N1 and N2 samples, respectively. In figure 4(c), a mesoporous honeycomb-like morphology indicates agglomeration of NiO NPs in N3 due to increased calcination temperature.

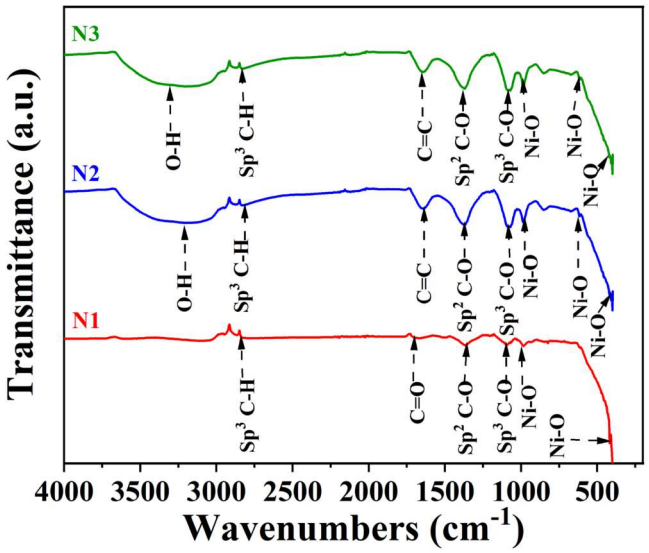

Figure 3. FT-IR spectra for the synthesized NiO NPs.

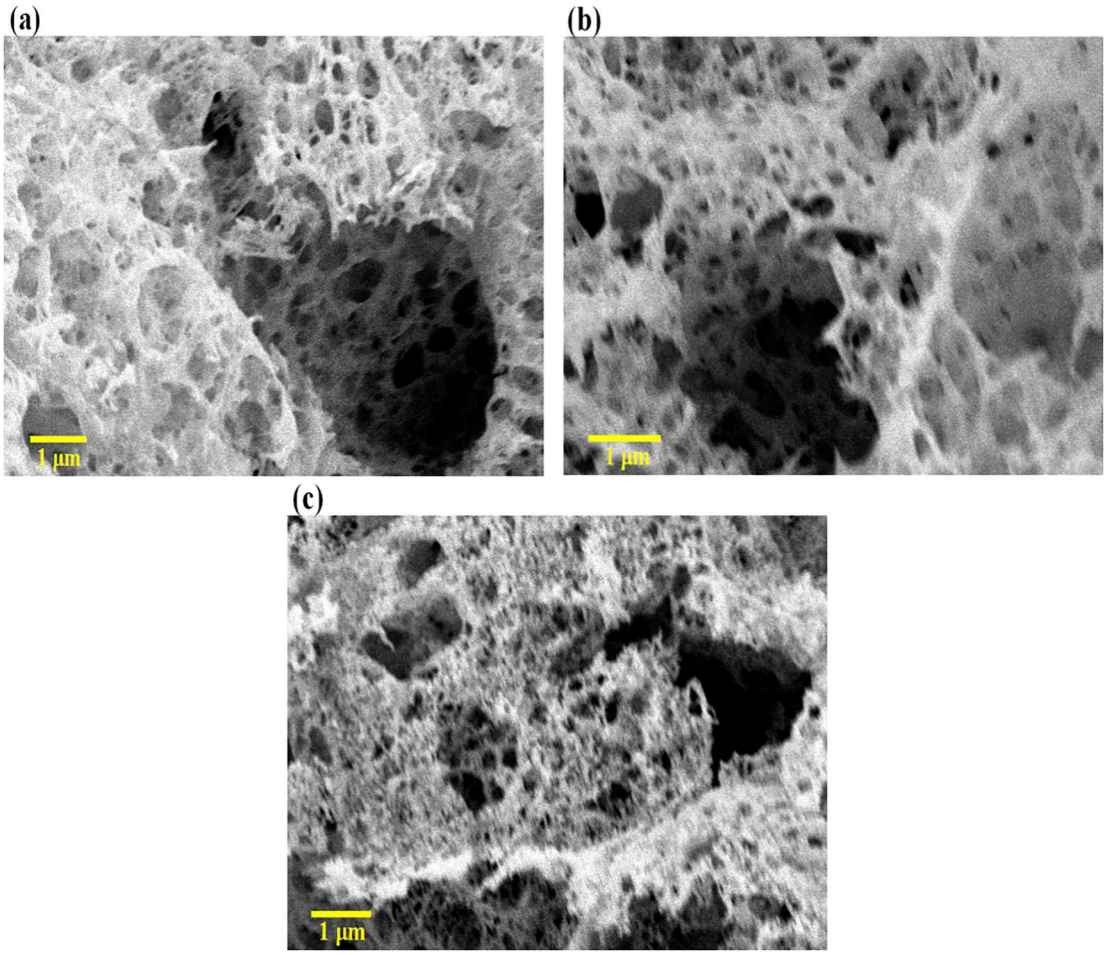

Figure 4. SEM images for NiO NPs calcined at different temperatures (a) 300 °C (N1), (b) 400 °C (N2), and (c) 500 °C (N3).

3.4. Electrical and optical properties studies

3.4.1. Photolumenescence (PL)

The strong response to PL shown in figure 5 shows that the honeycomb-like NiO NPs are good visible light emitters at room temperature [39]. The PL intensity increases as the calcination temperature is increased. The strong emission band peaks, however, occur at different wavelengths as observed at 432.0533 nm for the N1

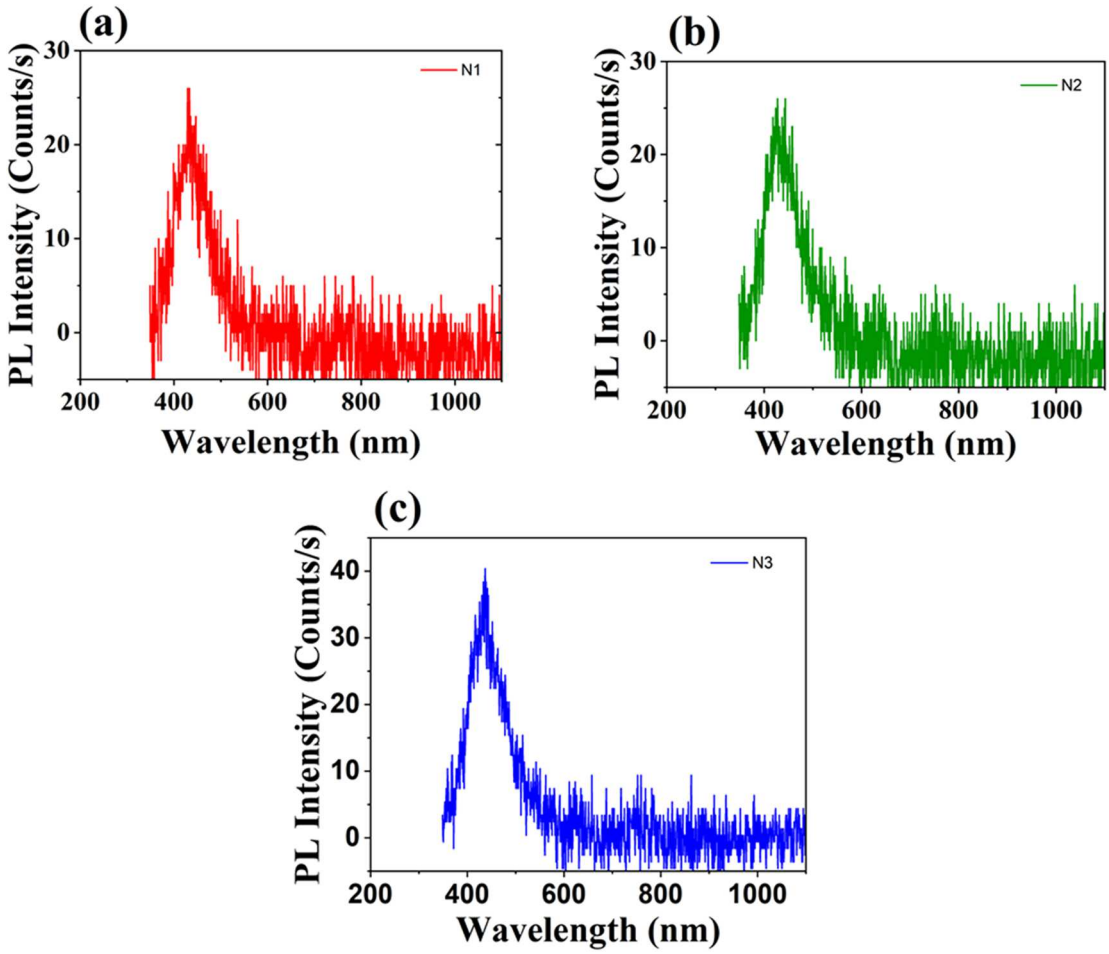

Figure 5. PL spectra for the biosynthesized NiO NPs (a) N1, (b) N2, and (c) N3 samples.

sample shown in figure 5(a), 427.8510 nm for N2 shown in figure 5(b), and 437.2079 nm for N3 sample shown in figure 5(c). This shows that there exists a blue and red-shift in the peak positions, that is attributed to the self-trapped exciton from electron–hole recombination which also indicates that the NiO latticess in the samples have oxygen vacancies [39, 40].

3.4.2. Absorbance and optical band energies

The reflectance spectra reduces towards the shorter wavelength region (350–300 nm), showing a blue shift (UV region) in absorption exhibited by the synthesized NiO NPs [13] as shown in figure 6(a). In this regard, all samples are observed to have an absorption edge at around 335 nm. It is observed that the reflectance increases with an increase in calcination temperature.

Using the Kubelka–Munk function F(R) in expressions 5 and 6, the absorbance was estimated, and from Expression 4, the spectra are shown in the inset of figure 6(a).

Tauc plots were drawn using Expression 5 to estimate the band gap of the biosynthesized NiO NP samples.

$$F(R) = \frac{\text{Absorption coefficient}}{\text{Scattering coefficient}} = \frac{k}{s} = \frac{(1-R)^2}{2R} \tag{5}$$

$$(F(R)h\vartheta)^n = A(h\vartheta - E_g) \tag{6}$$

where R is the percentage reflectance obtained from the DRS data, n is the type of optical transition. In this study, an allowed direct band gap (n = 2) was used. A is the proportionality constant, h is Planck's constant, ν is the Photons frequency, and E_g is the band gap [41], established using the linear fit method of *ORIGIN* software.

From the Tauc plots in figures 6(b), (c), and (d), band gap energies of 3.51 eV, 3.48 eV, and 3.43 eV were obtained for samples N1, N2, and N3, respectively. This showed that the band gap energies decreased with an increase in calcination temperature, which aligns well with the particle size variations established from the XRD results.

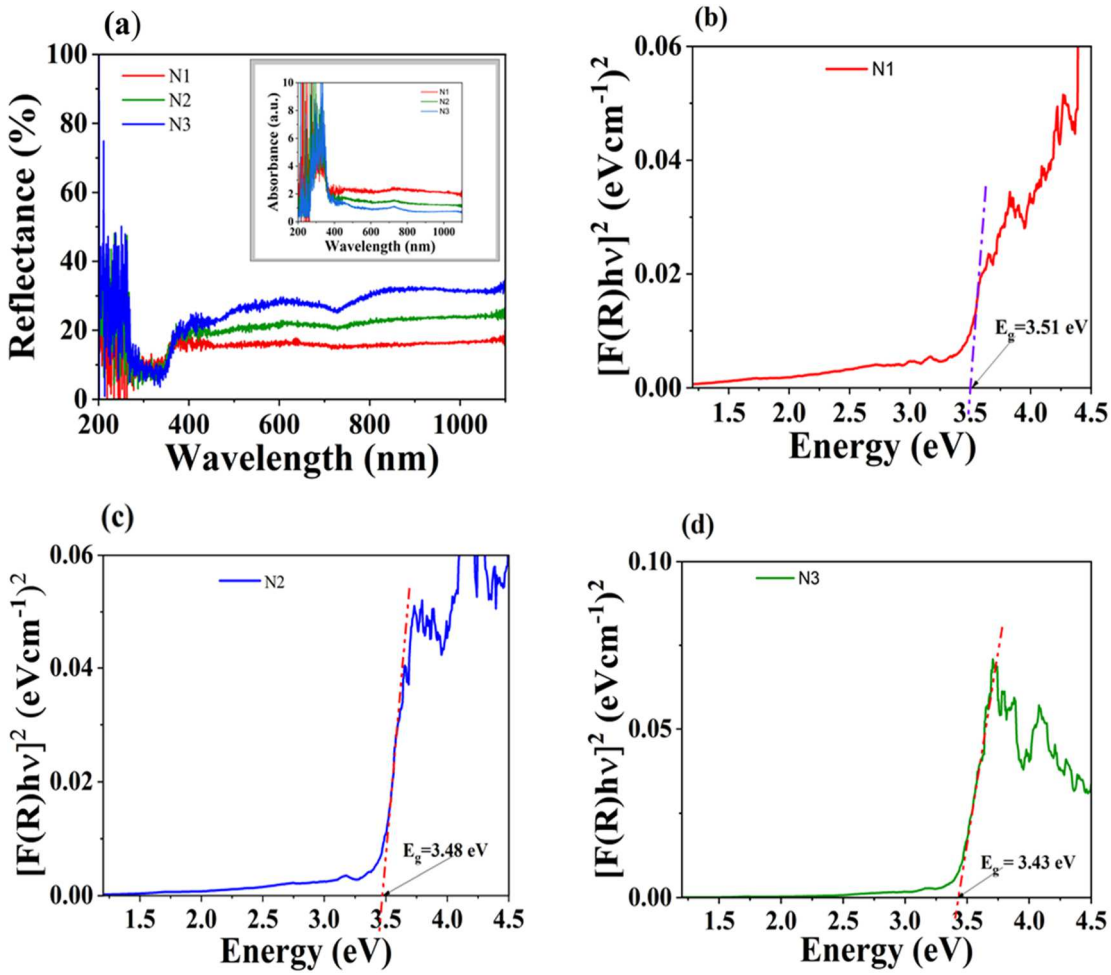

Figure 6. (a) Reflectance spectra with corresponding inset absorbance spectra for the NiO NPs synthesized at different calcination temperatures, (b) Tauc plot for N1, (c) Tauc plot for N2, and (d) Tauc plot for N3.

3.5. DSSC *J-V* performance tests

From figures 7(a) and (b), the highest short-circuit current (J_{sc}) of 2.05 mA cm^{-2} from the TiO_2-Pt cell setup was determined, whereas acurrent density of 0.113 mA cm^{-2} was determined for the TiO_2-NiO cell setup. The open-circuit voltages (V_{oc}) of 194.54 mV and 466.07 mV for the TiO_2-NiO and TiO_2-Pt cell setups, respectively were determined. The maximum power densities (P_{max}) from both cells, are shown in table 2. The the fill factor (*FF*) and efficiency (η) values for both cells were calculated using expressions described by Sharma *et al* [42], obtaining values shown in table 2.

The results indicate that NiO has potential for application as a counter electrode. The mesoporous honeycomb-like morphology exhibited in NiO provided a substantial surface area and pore volume, enabling the NiO electrode to have more contact with the iodide electrolyte, which facilitated ion diffusion at the counter electrode end of the DSSC.

The performance in the TiO_2-Pt is attributed to Pt's high conductivity and catalytic activity, which enhanced the DSSC performance compared to the TiO_2-NiO cell architecture with NiO as a counter-electrode.

A comparison of the findings with other novel research findings obtained from chemical and biosynthesis techniques indicates a relatively low performance from this study on the NiO counter electrode, but significantly higher compared to the performance of the biosynthesized CuO-based counter electrode, as shown in table 3.

3.6. Charge transport properties

The series resistance, R_S at the counter electrode/FTO interface, the charge transfer resistance, R_{CT} at the counter electrode/redox electrolyte interface, and the equivalent circuit capacitance were obtained using the potentiostat's data analysis (CS Studio6) software.

The resistance to charge transport at the Pt/FTO interface is represented by the Nyquist plot shown in figure 8(a). It is a semicircle whose trend matches well those obtained by Mujahid and Al-Hartomy [47]

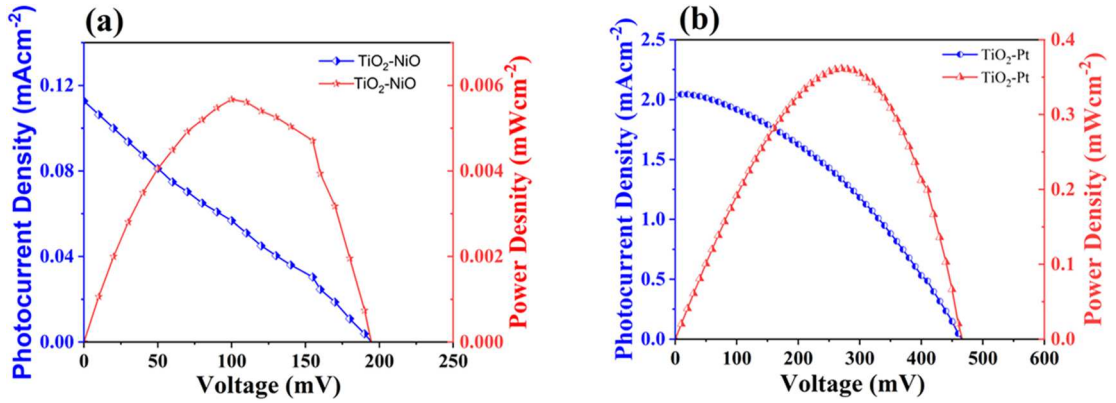

Figure 7. DSSC performances (a) the *J-V* characteristic of TiO_2-NiO with the corresponding power density, (b) the *J-V* characteristic for TiO_2-Pt with its power density.

Table 2. DSSC Performance of the two setups.

Cell Setup	Counter electrode	J_{sc} ($mAcm^{-2}$)	V_{oc} (mV)	P_{max} ($mWcm^{-2}$)	Fill Factor, FF	η (%)
TiO_2-NiO	NiO	0.113	194.54	0.0057	0.259	0.0057
TiO_2-Pt	Pt	2.05	466.07	0.3616	0.378	0.3616

indicating a series connection of the series resistance, $R_{S,}$ to a parallel connection of charge transfer resistance at the electrolyte/Pt/FTO interfaces, $R_{CT,}$ and a capacitance, C. The equivalent circuit is shown in the inset figure 8(a). The resistances are summarised in table 4. The resistance to charge transport at the TiO_2-NiO interface is represented by the Nyquist plot shown in figure 8(b). The equivalent circuit is shown in the inset of figure 8(b). Its trend matches well with those reported by Etefa *et al* [46] and Chen *et al* [45]. The R_{CT} for NiO as a counter electrode in the TiO_2-NiO DSSC was found to be 4.956×10^4 Ωcm^2, which is much higher than that obtained for the Pt counter electrode in the TiO_2-Pt DSSC (1205 Ωcm^2). The lower resistance obtained in the TiO_2-Pt cell correlates well with the good solar cell efficience in the Pt counter electrode compared to the NiO counter electrode. The poor performace in the NiO-TiO2 DSSC can be attributedto the charge recombination effects in the NiO nanostructure or weak bonding between the NiO and the FTO substrate [45]. However, the series resistance R_s in the NiO-TiO2 DSSC setup (41.78 Ωcm^2) is relatively small compared to that in the Pt-TiO2 counter electrode cell setup (64.07 Ωcm^2). The experiemental values are are in agreement to what was reported by Cheng *et al* [47], demonstrating that NiO has the potential to serve as a counter electrode in DSSCs. The performance in the NiO-TiO2 DSSC can be improved by dopping with an alkaline-earth metal [48].

3.7. DFT studies

3.7.1. Ground state structural properties

Figure 9(a) shows the lattice structure of NiO with FCC Fm-3m geometry in which the four oxygen (O) atoms are bonded to four Nickel (Ni) atoms, and the experimental lattice parameters for a primitive unit cell are a = b = c = 4.1853 Å. Figure 9(b) illustrates the variation of Total energy and lattice parameter of NiO at different optimization for DFT with and without Hubbard correction. The optimized lattice parameters were 4.1289, 4.1874, and 4.1933 Å for $U_d = 0$, 5, and 6 eV, respectively, with −368.1843, −368.1173, and −368.1074 Ry as corresponding total energies. The standard DFT underestimated the lattice parameter with 1.35% error as compared to our reported experimental value. This was greatly attributed to the failure of standard DFT based on the norm-conserving pseudo potentials, which are commonly known for underestimating the bond length in highly correlated materials such as NiO. However, on inclusion of the HUBBARD parameter U = 5 eV to the 3d-orbitals of Ni, the prediction of lattice parameter was improved to match the experimental value and then overestimated by 0.19% for $U_d = 6$ eV. This is in good agreement with the previous works on NiO, in which it was noted that GGA-PBE+U corrects the physical description of the structural parameters in the range of 4.17–4.20 Å.

3.7.2. Ground state electronic properties

The spin-resolved band structures and projected density of states (PDOS) were calculated on the intrinsic NiO to reveal its physical properties, as shown in figure 10. The band structures were all computed along the high

Table 3. A comparison of the performance of bioengineered NiO counter electrodes with other counter electrodes and their synthesis with the respective realized morphologies in DSSCs.

Counter Electrode	Synthesis method	Morphology	J_{sc} (mAcm^{-2})	V_{oc} (V)	Fill factor, FF	η (%)	References
NiO	Bio-engineering and spin coating	Honeycomb-like	0.113	0.1945	0.259	0.0057	This work
Pt			2.050	0.4661	0.3616	0.3780	This work
α-Fe_2O_3	Green synthesis and drop casting	Nanoflakes	7.000	0.3890	0.7530	2.0500	[43]
CuO	Green synthesis and drop casting		0.00018	0.1700		0.00018	[32]
NiO	Chemical Bath Deposition	Porous honeycomb-like	0.016	0.5500		0.0200	[44]
Pt			0.024	0.35		0.0100	[44]
P-NiO	Solvothermal	Flower-like nanosheets	15.830	0.7700	0.650	7.9500	[45]
NiO	Hydrothermal	Spherical nanoparticles	0.480	0.4600	0.342	0.7500	[46]
Nickel ntroprusside	Chemical technique and Doctor blade deposition	Cracked homogeneous nanoparticles	11.000	0.5300	0.455	2.6500	[6]
Pt			14.470	0.635	0.692	6.37	[6]

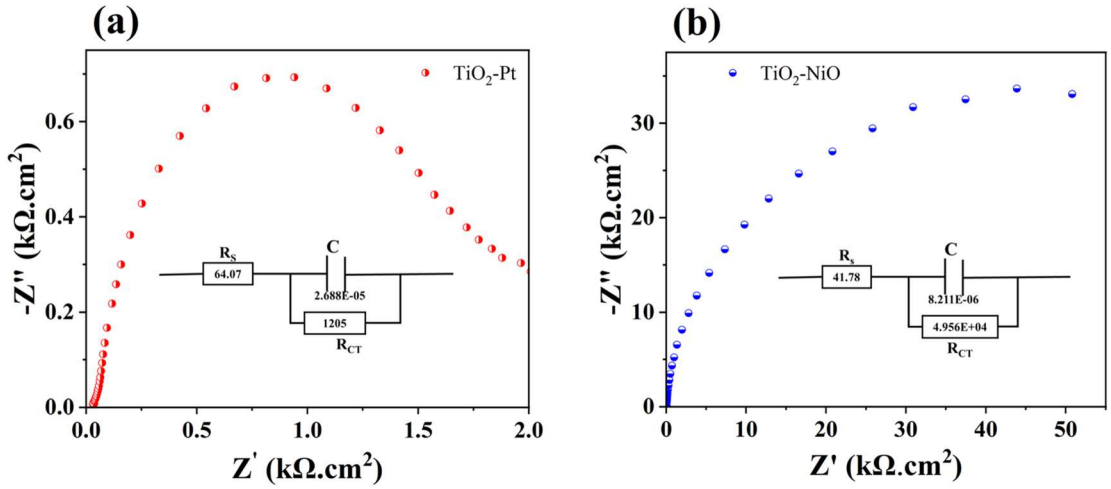

Figure 8. EIS Nyquist plots with corresponding equivalent circuits (inset); (a) TiO_2-Pt and (b) TiO_2-NiO.

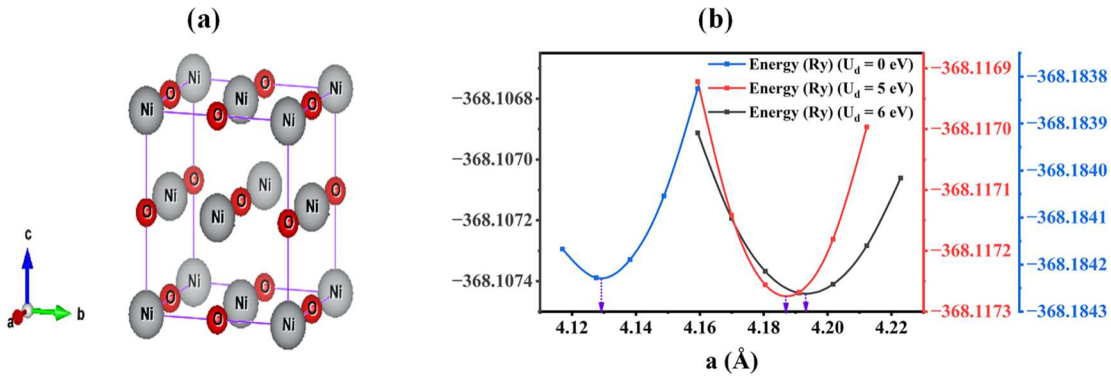

Figure 9. Shows (a) the unit cell of NiO and (b) the optimized lattice parameter for $U_d = 0$, 5, and 6 eV.

Table 4. EIS data on the TiO_2-Pt and the TiO_2-NiO DSSCs.

DSSC Setup	R_S (Ωcm^2)	R_{CT} (Ωcm^2)	C ($F\,cm^{-2}$)
TiO_2-Pt	64.07	1205.00	2.688×10^{-5}
TiO_2-NiO	41.78	4.956×10^4	8.211×10^{-6}

symmetry path of Γ-X-W-K-Γ-L-U-W for both the majority and minority spins (↑*and*↓). The GGA-PBE gave a metallic prediction of the NiO in which Ni-d and O-2p bands overlap and cross the Fermi level for both spins, giving a wrong band gap of 0 eV. This agrees with other studies on NiO, in which standard DFT notably gives an incorrect interpretation of its electronic structure as a metal with no band gap [29]. This is likely caused by the DFT's failure to deal with the strong electron correlations in the partially filled Ni-3d states. The standard DFT overdelocalizes these states, falsely predicting reduced on-site Coulombic repulsions, incorrectly positioning the orbitals around the Fermi level, thus significantly underestimating the band gap.

The addition of the on-site Hubbard correction (U) onto the Ni-3d states separates the upper from the lower Hubbard states, exposing a gap around the Fermi level. The filled and empty Ni-3d states are effectively shifted towards lower and higher energies, respectively, widening the band gap. For $U_d = 5$ eV, the top of the V.B. at −1.79 eV and bottom of the C.B. at 1.01 eV are both occurring at zone centre (Γ) for the spin down (↓) giving a direct optical band gap of 2.80 eV from the energy difference. In comparison with the PDOS, the O-2p states dominate the top of V.B. with little contribution from the Ni-3d states, and the bottom of C.B. is greatly dominated by the Ni-3d empty states for spin-down. Thus, the electron transit from O-2p states in the V.B. to the Ni-3d states, since electron transitions due to photons in AFM material like NiO occur within the same spin states. But the hybridization between the O-2p and Ni-3d states in the V.B. also predicts a small degree of

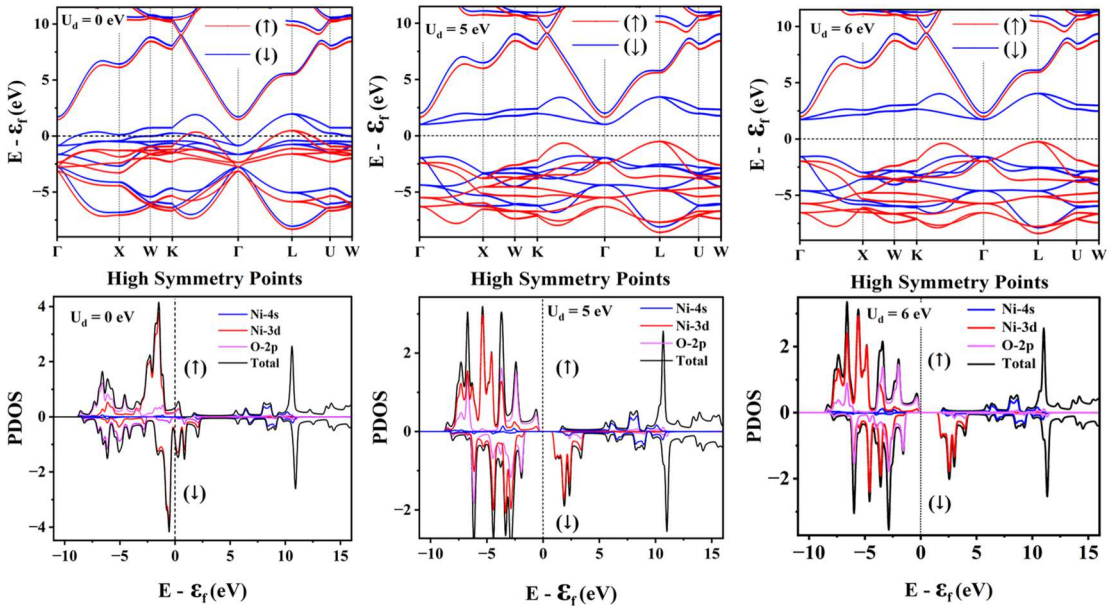

Figure 10. The calculated spin-polarized band structures of AFM NiO at $U_d = 0$, 5, and 6 eV and their corresponding projected density of states with the Fermi level set at zero.

covalency in NiO, as predicted by other studies. On the other hand, the up spin (↑) PDOS shows that the filled Ni-4s states contribute heavily at the bottom of the C.B., with O-2p states dominant at the top of the V.B. This transition is not possible since the Ni-4s orbitals are full; thus, the only possible electron transitions are within the spin-down states.

However, the predicted band gap of 2.80 eV for $U_d = 5$ eV was still slightly underestimated compared to the experimental value ($E_g = 3.43$ eV); hence, taking a higher value of U_d (6 eV) gave a better band gap of 3.24 eV. Increasing the U_d value to 6 eV further shifted the top of V.B. to −1.48 eV closer to the Fermi level, whereas the bottom of C.B. was shifted to 1.76 eV away from the Fermi level. This prediction reveals the p-type character of NiO, thus correcting the n-type prediction at $U_d = 5$ eV. The corresponding spin-polarized PDOS indicates a further reduction in the hybrization between the oxygen 2p and Nickel 3d states at the top of the V.B. It is reported that the band gap increases with U_d from 0 to 10 eV; however, at $U_d > 6eV$, the Ni-3d states are depleted, leaving the top of V.B. with majorly only O-2p states [28]. This prediction of NiO as purely a charge transfer material disagrees with the experimental data referred to as a Mott insulator, thus a computational limitation.

3.7.3. The dielectric function

The optical properties study reveals the interaction between materials and the UV-visible-infrared radiations. The dielectric function gives the linear behaviour of the NiO material when exposed to these electromagnetic radiations [49]. It is a complex function composed of real ($\varepsilon_1(w)$) and imaginary ($\varepsilon_2(w)$) parts as shown in (7).

$$\varepsilon(w) = \varepsilon_1(w) + i\varepsilon_2(w) \tag{7}$$

The other optical properties, such as refractive index ($n(w)$) and absorption coefficient ($\alpha(w)$) were calculated using equations (8) and (9).

$$n(w) = \sqrt{\frac{\sqrt{|\varepsilon_1(w)|^2 + |\varepsilon_2(w)|^2} + \varepsilon_1(w)}{2}} \tag{8}$$

$$\alpha(w) = \frac{w}{c}\sqrt{\frac{\sqrt{|\varepsilon_1(w)|^2 + |\varepsilon_2(w)|^2} - \varepsilon_1(w)}{2}} \tag{9}$$

Figures 11(a) and (b) show the spectra of the $\varepsilon_1(w)$ and $\varepsilon_2(w)$ up to a photon energy of 12.0 eV along the xx, yy, and zz directions, demonstrating the anisotropic behaviour of the AFM NiO. The $\varepsilon_1(w)$ exhibited a prominent peak at 3.22 eV, possibly due to a strong polarisation response. Beyond 4.0 eV, it significantly drops below zero, suggesting metallic behaviour, and beyond 6.0 eV, it remains almost constant, showing minimal dielectric response. The $\varepsilon_2(w)$ exhibited a strong energy peak around 3.30 eV, which corresponds to an electron transition from the O-2p filled orbitals within the V.B. to the C.B. Ni-3d empty orbitals, as shown in the PDOS.

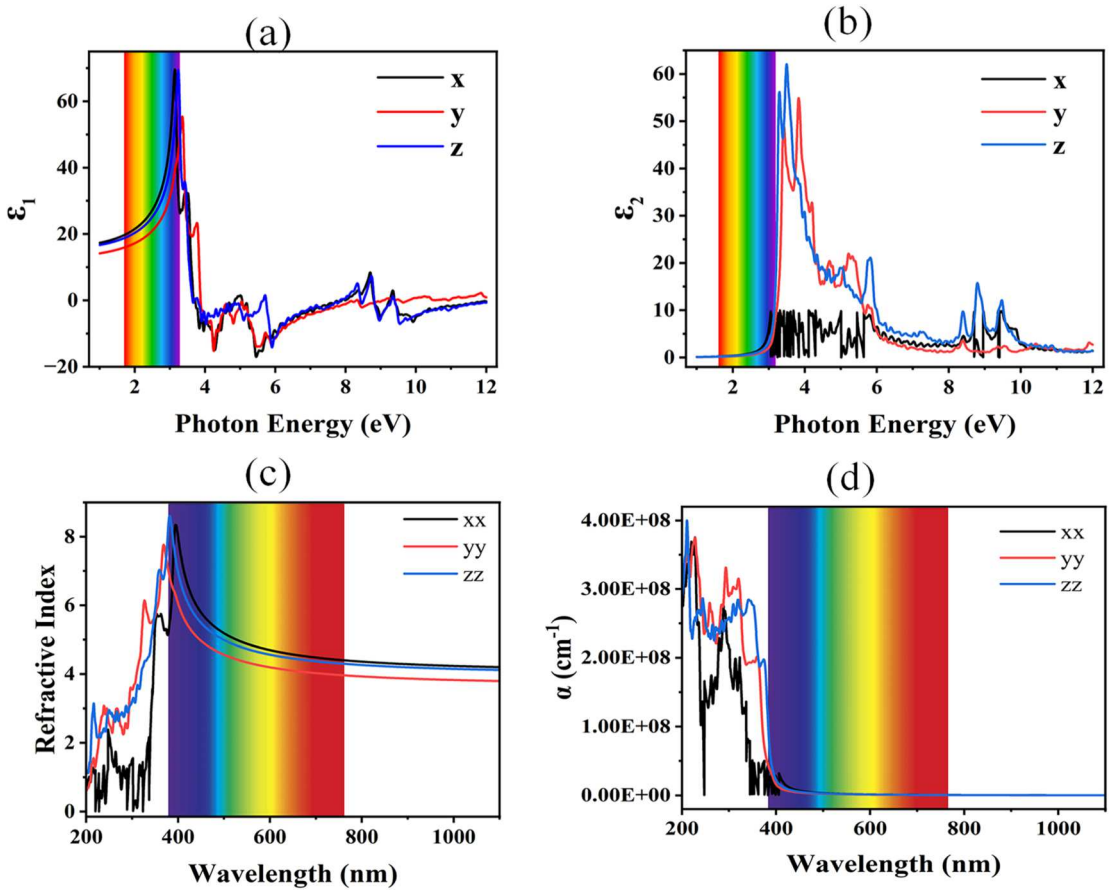

Figure 11. Shows the (a) real ($\varepsilon_1(w)$) and (b) imaginary ($\varepsilon_2(w)$) parts of the dielectric function, (c) refractive index spectra, and (d) absorption coefficient of the AFM NiO.

Other multiple peaks were observed at higher energies, indicating additional allowed electron transitions deep within the energy bands, as shown in figure 11(b).

Figure 11(c), the refractive index significantly increased in the UV region, peaking at around 400 nm in the Violet and UV region up to a magnitude $n \approx 8$. However, onwards the refractive index dropped sharply through the violet to the blue light and almost levels off around the red up to the infra-red light. This trend suggests optical transparency at longer wavelengths, followed by intense light–matter interaction close to the band edge. The absorption coefficient in figure 11(d) also exhibits sharp absorption edges in the UV region, with $\alpha > 10^8$ cm^{-1}, indicating effective photon absorption at energies higher than the bandgap. At longer wavelengths (wavelengths > 400), absorption decreases to almost zero, suggesting that there are minimal optical losses in the visible-NIR spectrum. This strongly agrees with our experimental results on PL and absorption taking place in the UV region (see figures 5 and 6) and previous computational works on NiO [49, 50]. The small anisotropies in all optical parameters in the x, y, and z directions could be caused by lattice distortions due to its inherent anti-ferromagnetic ordering and electronic correlation effects in the DFT+U framework [51]. A prospective contender for optoelectronic, photocatalytic, and photovoltaic applications, our results demonstrate that NiO combines substantial UV light absorption with good optical transparency in the visible–NIR range.

4. Conclusions and further work

NiO NPs were biosynthesized using Bamboo shoot juice plant extract as a capping and reducing agent. The XRD showed highly crystalline NiO was obtained with a cubic FCC structure and a Ni-O bonding on the FT-IR spectra, showing plant protein interaction with Nickel nitrate, reducing it to NiO NPs. The SEM images show that a soft honeycomb-like morphology was successfully realized in the study. The synthesized NiO NPs had an optical response to Photoluminescence and showed absorbance of UV region light, realizing reduced band gap energies with increased calcination temperatures.

Though the n-p DSSC (TiO_2-NiO) performance is lower than that of the n-DSSC (TiO_2-Pt) DSSC, developing composite materials and doping of NiO with alkaline-earth metal can improve its performance as a counter electrode.

The honeycomb-like structure developed in this study can also be tested for symmetrical supercapacitor applications as a positive electrode. Further, the effect of precursor molar concentrations and pH variations on the NiO NPs' morphology using bamboo shoot extract can be studied.

The DFT calculated lattice parameters using on-site Hubbard correction were in agrrement with experimental values. Further, the DFT calculations on the electronic properties revealed the p-type semiconductor of NiO, of direct band gap at Γ for spin-down, in agreement with experimental value. The projected density of states revealed that the Ni-4s dominates the spin-up C.B. minima and the Ni-3d dominates the spin-down C.B. minima, while the O-2p states dominate the V.B. maxima for both spins. NiO exhibited optical anisotropic with an absorption edge at 400 nm, depicting low optical losses in the visible-NIR spectrum. This optical anisotropy property is attributed to NiO exhibiting anti ferromagnetic ordering and DFT+U electronic correlation effects.

Although lattice parameters were successfully captured by DFT+U, the band gap was still underestimated, suggesting that many-body perturbation theory (GW) or more advanced functional such as hybrid, need to be explored to further improve the electronic interpretations.

Acknowledgments

This work was carried with support from Kyambogo University Competitive Research Grants (10^{th} Call), for whom we are grateful. The correspondin Author acknowledges support from UNESCO-TWAS financed by the German Federal Ministry of Education and Research (BMBF) (**No. 24-167 RG/PHYS/AF/AC_I—FR3240339180**). The views expressed herein do not necessarily represent those of UNESCO-TWAS, BMBF, or its Board of Governors.

Conflict of interest

The authors declare that there is no conflict of interest regarding the publication of this article.

Data availability statement

All data that support the findings of this study are included within the article (and any supplementary files).

Supplementary information

Not applicable.

Ethical approval

Not applicable.

Author contributions

Stella Nasejje
Conceptualization (equal), Data curation (lead), Formal analysis (lead), Investigation (lead), Methodology (lead), Software (equal), Validation (equal), Writing – original draft (lead), Writing – review & editing (lead)

Emmanuel Mushebo
Conceptualization (equal), Data curation (equal), Formal analysis (equal), Investigation (equal), Methodology (equal), Validation (equal), Visualization (equal), Writing – original draft (equal), Writing – review & editing (equal)

Denise Joanitah Birabwa
Conceptualization (equal), Data curation (equal), Formal analysis (equal), Funding acquisition (equal), Investigation (equal), Methodology (equal), Project administration (equal), Resources (equal), Supervision (equal), Validation (equal), Writing – original draft (equal), Writing – review & editing (equal)

Mmantsae Diale 0000-0002-6035-6688
Conceptualization (supporting), Formal analysis (supporting), Investigation (supporting), Methodology (supporting), Supervision (supporting), Validation (supporting), Writing – original draft (supporting), Writing – review & editing (supporting)

Emma Panzi Mukhokosi 0000-0001-9229-3821
Conceptualization (lead), Data curation (equal), Formal analysis (equal), Funding acquisition (lead), Investigation (equal), Methodology (equal), Project administration (lead), Resources (equal), Supervision (lead), Writing – original draft (supporting), Writing – review & editing (lead)

References

[1] Nasejje S, Mukhokosi E P, Diale M and Velauthapillai D 2024 Device architectures for photoelectrochemical water splitting based on hematite: a review *Discov. Mater.* **4** 44
[2] Yuan Y and Wan C 2022 Dual Application of waste grape skin for photosensitizers and counter electrodes of dye-sensitized solar cells *Nanomaterials* **12** 1–16
[3] Shahpari M, Behjat A, Khajaminian M and Torabi N 2015 The influence of morphology of hematite (a -Fe2O3) counter electrodes on the efficiency of dye-sensitized solar cells *Sol. Energy* **119** 45–53
[4] Nasejje S, Mukhokosi E P and Diale M 2025 A dye-sensitized solar cell based on an *in situ* hydrothermally grown hematite photo-anode *MRS Adv.* **10** 2473–8
[5] Senin N A H, Rummaja I D, Idris M I, Napiah Z A F M, Ramlee R H, Rashid M and Bradley L 2024 Analysis of nickel oxide as a counter electrode for dye-sensitized solar cells using OghmaNano software *Int. J. Power Electron. Drive Syst.* **15** 1218–26
[6] Rahman M M 2021 Low-cost and efficient nickel nitroprusside/graphene nanohybrid electrocatalysts as counter electrodes for dye-sensitized solar cells *Materials (Basel)* **14** 6563
[7] Zhu K, Mul G and Huijser A 2024 Dye-sensitized NiO photocathodes: research progress, current mechanistic understanding, and research perspectives *Chem. Phys. Rev.* **5** 021305
[8] Hashem M, Saion E, Al-hada N M, Kamari H M, Shaari A H, Talib Z A, Paiman S B and Kamarudeen M A 2016 Fabrication and characterization of semiconductor nickel oxide (NiO) nanoparticles manufactured using a facile thermal treatment *Results Phys* **6** 1024–30
[9] Qin Y X, Yang Z Z, Wang J J, Xie Z Y, Cui M Y, Tian C M, Du Y G and Zhang K H L 2018 Epitaxial growth and band alignment of p-NiO/n-Fe2O3 heterojunction on Al2O3 *Appl. Surf. Sci.* **464** 488–93
[10] Kadam S A, Kadam K P, Maria C S, Ma Y, Molane A C, Lolage S A, Patil V B and More P D 2024 Microporous α -Fe2O3@NiO heterostructures synthesized for enhanced supercapacitor performance *Chem. Sel.* **9** e202302376
[11] Ganesh V, Haritha L, Anis M, Shkir M, Yahia I S, Singh A and Alfaify S 2018 Structural, morphological, optical and third order nonlinear optical response of spin- coated NiO thin films: an effect of N doping *Solid State Sci.* **86** 98–106
[12] Ren X, Guo C, Xu L, Li T, Hou L and Wei Y 2015 Facile Synthesis of hierarchical mesoporous honeycomb-like NiO for aqueous asymmetric supercapacitors *Appl. Mater. Interfaces* **7** 19930–40
[13] Hong S J, Mun H J, Kim B J and Kim Y S 2021 Characterization of nickel oxide nanoparticles synthesized under low temperature *Micromachines* **12** 1168
[14] Wang J, Zhou Q, Lu Z, Wei Z and Zeng W 2019 The novel 2D honeycomb-like NiO nanoplates assembled by nanosheet arrays with excellent gas sensing performance *Mater. Lett.* **255** 126523
[15] Nagamuthu S and Ryu K-S 2019 Synthesis of Ag/NiO honeycomb structured nanoarrays as the electrode material for high performance asymmetric supercapacitor devices *Sci. Rep.* **9** 4864
[16] Iqbal J, Abbasi B A, Mahmood T, Hameed S, Munir A and Kanwal S 2019 Green synthesis and characterizations of nickel oxide nanoparticles using leaf extract of Rhamnus virgata and their potential biological applications *Appl. Organometallic Chem.* **33** e4950
[17] Barzinjy A A, Hamad S M, Aydın S, Ahmed M H and Hussain F H S 2020 Green and eco-friendly synthesis of nickel oxide nanoparticles and its photocatalytic activity for methyl orange degradation *J. Mater. Sci., Mater. Electron.* **31** 11303–16
[18] Iqbal J *et al* 2020 Phytogenic Synthesis of nickel oxide nanoparticles (NiO) using fresh leaves extract of rhamnus triquetra (Wall.) and investigation of Its multiple *In Vitro* biological potentials *Biomedicines* **8** 117
[19] John J, Thomas L, Kumar B R, Kurian A and George S D 2015 Shape dependent heat transport through green synthesized gold nanofluids *J. Phys. D: Appl. Phys.* **48** 335301
[20] Mehta B K, Chhajlani M and Shrivastava B D 2017 Green synthesis of silver nanoparticles and their characterization by XRD *IOP Conf. Series: Journal of Physics: Conf. Series* 836 (IOP Publishing) 012050
[21] Jassim S M, Abd M A and Hammed I A 2023 Green synthesis of nickel oxide nanoparticles using syzygium aromatic extract: characterization and biological applications *Al-Bahir J. Eng. Pure Sci.* **2** 7
[22] Fardood S T, Ramazani A and Moradi S 2017 A novel green synthesis of nickel oxide nanoparticles using Arabic gum *Chem. J. Mold. Gen. Ind. Ecol. Chem* **12** 115–8
[23] Sani A *et al* 2021 Floral extracts-mediated green synthesis of NiO nanoparticles and their diverse pharmacological evaluations *J. Biomol. Struct. Dyn.* **39** 4133–47
[24] Kalita C, Ganguly M and Devi A 2018 Biosynthesis of silver nanoparticles by using edible bamboo shoots with high antioxidant properties *Res. J. Life Sci. Bioinformatics, Pharm. Chem. Sci.* **4** 652–66
[25] Jayarambabu N, Velupla S, Akshaykranth A, Anitha N and Rao T V 2023 Bambusa arundinacea leaves extract - derived Ag NPs: evaluation of the photocatalytic, antioxidant, antibacterial, and anticancer activities *Appl. Phys. A Mater. Sci. &Processing* **129** 13
[26] Giannozzi P *et al* 2020 Quantum ESPRESSO toward the exascale *J. Chem. Phys.* **152** 154105
[27] Burke K, Perdew J P and Ernzerhof M 1997 Why the generalized gradient approximation works and how to go beyond it *Int. J. Quantum Chem.* **61** 287–93
[28] Gebhardt J and Elsässer C 2023 DFT with corrections for an efficient and accurate description of strong electron correlations in NiO *J. Phys. Condens. Matter* **35** 205901
[29] Li R, Xin D, Huang S, Wang Z, Huang L and Zhou X 2018 A full potential all-electron calculation on electronic structure of NiO *Chinese J. Phys.* **56** 2829–36

[30] Samat M H, Ali A M M, Taib M F M, Hassan O H and Yahya M Z A 2016 Results in physics hubbard U calculations on optical properties of 3 d transition metal oxide *Results Phys.* **6** 891–6
[31] Mukhokosi E P, Mohammed T, Loyce N, Botha N L, Maaza M and Velauthapillai D 2024 Co-sensitization effect of chlorophyll and anthocyanin on optical absorption properties and power conversion efficiency of dye-sensitized solar cells *J. Korean Phys. Soc.* **84** 858–69
[32] Mukhokosi E P, Tenywa S, Botha N L, Azizi S, Seopelad M and Maaza M 2025 Green synthesis of CuO nanoparticles from cucurbita maxima leaf extract; a platinum free counter electrode for dye sensitized solar cells *J. Niger. Soc. Phys. Sci.* **7** 2309
[33] Balabye S, Mushebo E, Nasejje S, Egor M and Mukhokosi P E 2025 Green synthesis of ZnO nanoparticles for DSSC photoanode: a joint experimental and density functional theory study *Mater. Res. Express* **12** 105004
[34] Babar N and Joya K S 2020 Spray-coated thin-film Ni-Oxide Nano fl akes as single electrocatalysts for oxygen evolution and hydrogen generation from water splitting *ACS Omega* **5** 10641–50
[35] Taskopru T, Turan E and Zor M 2015 Characterization of NiO films deposited by homemade spin coater *Int. J. Hydrogen Energy* **41** 6965–71
[36] Landolsi Z, Assaker I B, Chtourou R and Ammar S 2018 Photoelectrochemical impedance spectroscopy of electrodeposited hematite α-Fe2O3 thin films: effect of cycle numbers *J. Mater. Sci., Mater. Electron.* **29** 8176–87
[37] Ahmed M R, Ali H M and Hasaneen M F 2021 Influence of different types of substrates on the physical properties of CdSe films *Phys. B Phys. Condens. Matter* **608** 412747
[38] Kumar A and Yadav K 2017 Optical properties of nanocrystallite films of α-Fe2O3 and α-Fe2−xCrxO3 (0.0 x 0.9) deposited on glass substrates *Mareials Res. Express* **4** 075003
[39] Govindarajan B, Palanimuthu R and Manikandan K M 2019 Influence of Mg doping in magnetic properties of NiO nanoparticles and its electrical applications *J. Mater. Sci., Mater. Electron.* **30** 6519–27
[40] Musevi S J, Aslani A, Motahari H and Salimi H 2016 Offer a novel method for size appraise of NiO nanoparticles by PL analysis: Synthesis by sonochemical method *J. Saudi Chem. Soc.* **20** 245–52
[41] Mukhokosi E P, Maaza M, Tibenkana M and Botha N L 2023 Optical absorption and photoluminescence properties of cucurbita maxima dye adsorption on TiO2 nanoparticles *Mater. Res. Express* **10** 046203
[42] Sharma K, Sharma V and Sharma S S 2018 Dye-sensitized solar cells : fundamentals and current status *Nanosci. Res. Lett.* **13** 381
[43] Mukhokosi E P, Mushebo E, Nassejje S, Botha N L, Velauthapillai D and Maaza M 2025 Green synthesis of hematite nano flakes and their application as a counter electrode in dye-sensitized solar cells *Nat. Portifolio* **15** 19837
[44] Yadav A T, Magar P P, Kadam V S, Jagtap C V and Pawar C S 2016 Chemically deposited nickel oxide as counter electrode for dye sensitized solar cell *J. Mater. Sci., Mater. Electron.* **27** 12297–301
[45] Chen Y L, Huang Y J, Yeh M H, Fan M S, Lin C T, Chang C C, Ramamurthy V and Ho K C 2022 Nanoflower-like P-doped nickel oxide as a catalytic counter electrode for dye-sensitized solar cells *Nanomaterials* **12** 4036
[46] Etefa H F, Kumar V, Dejene F B, Efa M T and Jule L T 2023 Modification of flexible electrodes for P-type (Nickel Oxide) dye-sensitized solar cell performance based on the cellulose nanofiber film *ACS Omega* **8** 15249–58
[47] Mujahid M and Al-Hartomy O A 2022 The Effects of Pt-Doped TiO2 nanoparticles and thickness of semiconducting layers at photoanode in the improved performance of dye-sensitized solar cells *Materials (Basel)* **15** 7941
[48] Liu Y *et al* 2020 Highly conductive alkaline-earth metal electrodes: the possibility of maintaining both low work function and surface stability for organic electronics *Adv. Opt. Mater.* **8** 2000206
[49] Ahmed T Y, Saeed S R and Aziz S B 2025 Enhancing electronic and optical properties of NiO using Cu-doping: a DFT approach for band gap reduction *Oxford Open Mater. Sci.* **5** itaf009
[50] Zhang R, Jian W, Yang Z-D and Bai F-Q 2020 Insights into the photocatalytic mechanism of the C4N/MoS2 heterostructure: a first-principle study *Chinese Chem. Lett.* **31** 2319–24
[51] Bala N, Singh H K, Verma S and Rath S 2020 Magnetic-order induced effects in nanocrystalline NiO probed by Raman spectroscopy *Phys. Rev. B* **102** 024423